Journal Pre-proofs

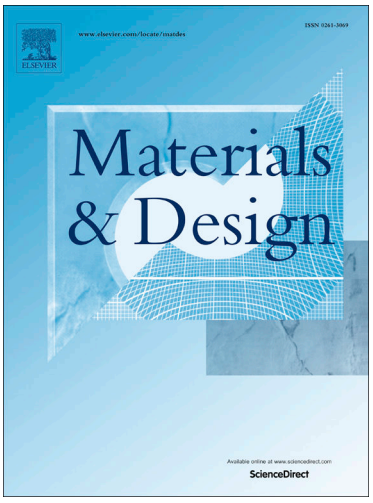

Design optimization of multifunctional metamaterials with tunable thermal expansion and phononic bandgap

Xing Zhang, Hongling Ye, Nan Wei, Ran Tao, Zhen Luo

PII: S0264-1275(21)00544-X
DOI: https://doi.org/10.1016/j.matdes.2021.109990
Reference: JMADE 109990

To appear in: *Materials & Design*

Received Date: 18 May 2021
Revised Date: 6 July 2021
Accepted Date: 14 July 2021

Please cite this article as: Zhang, X., Ye, H., Wei, N., Tao, R., Luo, Z., Design optimization of multifunctional metamaterials with tunable thermal expansion and phononic bandgap, *Materials & Design* (2021), doi: https://doi.org/10.1016/j.matdes.2021.109990

tunable thermal expansion and phononic bandgap

Xing Zhang[a], Hongling Ye[a,] *, Nan Wei[a], Ran Tao[b], Zhen Luo[c]

a Faculty of Materials and Manufacturing, Beijing University of Technology, Beijing, 100124, PR China
b Institute of Advanced Structure Technology, Beijing Institute of Technology, Beijing, 100081, PR China
c The School of Mechanical and Mechatronic Engineering, University of Technology Sydney, 15, NSW 2007, Australia

***Corresponding author:** yehongl@bjut.edu.cn (Professor H.L. Ye).

Abstract: Metamaterials have been extensively investigated owing to their unusual properties. However, the design of multifunctional metamaterials requires further investigation. This study focused on the design of three-dimensional (3D) metamaterials to achieve tunable negative thermal expansion and phononic bandgap properties. First, the independent continuous mapping (ICM) topology optimisation method was applied to create metamaterial microstructures with negative thermal expansion properties based on the multi-scale asymptotic homogenisation theory. Secondly, the conceptual structure from the topology optimisation was reconstructed and parameterized to achieve the desired phononic bandgap widths under negative thermal expansion, using a surrogate model-based optimisation method. Both the negative coefficient of thermal expansion and phononic bandgaps were verified through numerical simulations. The results reveal that, by selecting appropriate parameters, the designed metamaterials can have both a negative coefficient of thermal expansion and a maximum bandgap width ratio. The proposed method provides an important reference for the rational design of multifunctional metamaterials.

Keywords: Multifunctional metamaterials; Topology optimization; Surrogate model-based optimization; Negative thermal expansion; Phononic bandgaps

1. Introduction

Metamaterials are artificially engineered cellular composite materials that are structured to have extraordinary properties beyond those of most naturally occurring materials. The properties of metamaterials are determined by their rationally designed and periodically arranged microstructures, instead of the chemical composition of their base materials [1]. Research on metamaterials has recently attracted extensive interest, and such materials can be customized to provide a range of tunable multifunctionalities, which has unlimited potential for the development of various applications. For example, two ordinary solid materials with different positive coefficients of thermal expansion (CTE) can be used to generate new metamaterials that exhibit both effective negative thermal expansion (NTE) coefficients and phononic bandgap properties [2]. The negative thermal expansion property can be used for the thermal compensation of machine tools, which reduces the dependence on electronic control systems [3, 4]. Metamaterials with bandgap functions also play an important role in the design of vehicles [5] and large astronomical telescopes [6]. Therefore, this study focused on the systematic design of multifunctional metamaterials to achieve negative thermal expansion using topology optimization, and phononic bandgaps using surrogate model-based optimization, which are novel contributions. The design of multifunctional metamaterials provides a reference for maintaining device stability in environments wherein vibration is coupled with thermal loads, such as in hypersonic vehicles [7].

There are three design methods for obtaining metamaterials with negative thermal expansion according to the principle of deformation: coordinate deformation of double-layer beam structures, combined deformation of multi-link structures, and topology optimisation. The deformation principle of the double-layer beam structure is that the two-layer beams of different CTE materials undergo coordinated deformation and shrink in a certain direction when the temperature rises [8–13]. Extreme thermal expansion deformation can be achieved by combining double-layer beam structures with chiral structures [14, 15]. The deformation principle of the multi-link structures is that the triangular link unit shrinks in the vertical direction and is driven by a high thermal expansion rod [16–21]. Concave multi-link structures have the characteristics of low weight and high strength. The two above-mentioned types of structures can be easily designed based on experience, owing to their simple deformation principle. The topology optimisation method can be applied to generate various novel geometric architectures and create different thermoelastic materials and structures [22–26].

Topology optimisation provides a high degree of freedom in the design of structural elements by optimising the elements' effective properties. This method has the unique advantage of considering the periodic effect of a set of microstructures on the performance of the composite structure at the beginning of design. Thus far, the typical methods for topology optimisation mainly include the homogenisation method [27], solid isotropic material with penalisation (SIMP) method [28–31], level set method [32–34], phase field method [35], moving morphable components (MMC) method [36], and independent continuous mapping (ICM) method [37–39]. Among these methods, ICM facilitates multi-material modelling because the independent continuous variable unifies various types of variables. Element behaviour is associated with an independent continuous variable that is independent of any property of the material. The relationship between the material properties and topological variables was established using the filter function. Additionally, there are many types of ICM methods that provide flexible choices for designs subjected to different conditions [40].

The design of multifunctional metamaterials, such as the combination of negative/zero thermal expansion with a negative Poisson's ratio [41–43], multi-steady-state structures [44, 45], or variable-stiffness metamaterials with origami [46], has gradually become a development trend. However, there are few

studies on combining phonon bandgaps and negative thermal expansion to achieve multifunctional metamaterials. The propagation of waves at specific frequencies can be significantly suppressed by periodically arranging the metamaterial units, and the bandgap can be regulated by changing the shape of the unit. Metamaterials with bandgaps mainly have one-dimensional [47, 48], two-dimensional [49–53], and three-dimensional morphologies [54–56] according to the periodic conditions. Most existing studies focus on the absolute bandgaps of two-dimensional and three-dimensional metamaterials. In early studies, solid columns were inserted into the metamaterial matrix to absorb the elastic waves. The principle can also be applied to structures with cavities; therefore, negative thermal expansion metamaterials obtained by topology optimisation also have good potential for use in bandgap regulation. Presently, there are many ways toward optimising the bandgap design of metamaterials, such as parameter optimisation [57], topology optimisation [58–60], and machine learning [61]. In this study, both topology optimisation and parameter optimisation methods were integrated as a hierarchical architecture to implement multifunctional metamaterials.

This paper proposes a new design optimisation method for creating three-dimensional metamaterials with both negative thermal expansion and phononic bandgaps. First, the ICM topology optimisation method is proposed to generate a structure with negative thermal expansion. Through parametric modelling, the topological conceptual structure was further designed to have a bandgap function. The low-frequency characteristics of the metamaterials were investigated based on the Bloch theorem. Then, the final structures were obtained using surrogate-model optimisation to broaden the bandgap width under a specified negative thermal expansion characteristic. The results obtained by the proposed method provide an important reference for the design of multifunctional metamaterials to control the temperature and mechanical vibration.

2. Theory and principle

2.1. Homogenization theory

In this study, the homogenisation theory was introduced to investigate the thermoelastic behaviour of metamaterials. In theory, the mechanical properties of a material are assumed to follow a linear relationship. The metamaterials were assumed to be arrayed with infinite periodic units. The asymptotic expansion of the thermoelastic equation is carried out using perturbation theory to obtain the relationship between the effective properties and the local strain caused by thermal expansion, which is expressed as follows:

$$C_{ijkl}^{H} = \frac{1}{|Y|}\int_{Y}\left(C_{ijkl} - C_{ijpq}\frac{\partial \chi_{p}^{kl}}{\partial y_{q}}\right)\mathrm{d}Y \tag{2}$$

$$\beta_{ij}^{H} = \frac{1}{|Y|}\int_{Y}\left(C_{ijkl}\alpha_{kl} - C_{ijkl}\frac{\partial M_{k}}{\partial y_{l}}\right)\mathrm{d}Y \tag{3}$$

$$\alpha_{ij}^{H} = (C_{ijkl}^{H})^{-1}\beta_{kl}^{H} \tag{4}$$

where C_{ijkl}^{H}, β_{ij}^{H}, and α_{ij}^{H} are the effective elastic tensor, effective thermal stress tensor, and effective coefficient of thermal expansion, respectively; C_{ijkl} and α_{kl} are the elastic tensor and CTE of the materials, respectively; χ_{p}^{kl} and M_{k} are the local displacement fields of the metamaterial unit.

2.2. ICM model for topology optimization

To achieve a negative thermal expansion property, the metamaterials consist of at least three phases: void phase, low thermal expansion phase, and high thermal expansion phase. In the ICM method, the properties

of the three-phase material elements are determined by two independent continuous topological variables, namely, $\boldsymbol{r}$ and $\boldsymbol{s}$. The element material properties were identified using the filter function, as follows:

$$C_i = f_{rC}(r_i)\left[C^{(1)}\left(1-f_{sC}(s_i)\right)+C^{(2)}f_{sC}(s_i)\right] \tag{5}$$

$$\alpha_i = f_{r\alpha}(r_i)\left[\alpha^{(1)}\left(1-f_{s\alpha}(s_i)\right)+\alpha^{(2)}f_{s\alpha}(s_i)\right] \tag{6}$$

$$w_i = f_{rw}(r_i)\left[w^{(1)}\left(1-f_{sw}(s_i)\right)+w^{(2)}f_{sw}(s_i)\right] \tag{7}$$

where $f_{rC}(r_i)$, $f_{rC}(s_i)$, $f_{r\alpha}(r_i)$, $f_{r\alpha}(s_i)$, $f_{rw}(r_i)$, and $f_{rw}(s_i)$ are the filter functions used to identify the element elastic modulus C_i, element coefficient of thermal expansion α_i, and element weight w_i, respectively. Superscripts (1) and (2) represent the number of materials. The element is void when $r_i = 0$. The element is solid when $r_i = 1$. When $r_i = 1$, $s_i = 0$ or $s_i = 1$ indicates that the element i is material described by Eq. (1) or Eq. (2), respectively. The filter functions are expressed in the form of a power function, as follows:

$$\begin{aligned} &f_{rC}(r_i) = r_i^3, f_{r\alpha}(r_i) = r_i^3, f_{rW}(r_i) = r_i \\ &f_{rC}(s_i) = s_i^3, f_{r\alpha}(s_i) = s_i^3, f_{rW}(s_i) = s_i \end{aligned} \tag{8}$$

Then, the optimisation model can be established with the minimum effective thermal stress tensor as the objective function, subject to the effective elastic modulus and weight fraction. To avoid numerical instability phenomena, such as node connections, the effective elastic modulus of the structure must have a lower limit. According to Eq. (3), the effective CTE of the metamaterial unit is linearly related to the thermal stress tensor. The thermal stress, which is considered as the objective function, can achieve a negative CTE and avoid an extremely low effective elastic modulus. To ensure the lightweight design space of the metamaterial, unnecessary material should be removed. Then, the optimisation model can be expressed as follows:

$$\begin{aligned} &\text{Find} \quad \boldsymbol{r},\boldsymbol{s} \in E^N \\ &\text{Min} \quad \beta(\boldsymbol{r},\boldsymbol{s}) \\ &\text{s.t.} \ C_{ijkl}^{\mathrm{H}}(\boldsymbol{r},\boldsymbol{s}) \geq \underline{C} \\ &\qquad W(\boldsymbol{r},\boldsymbol{s}) \leq \overline{W} \\ &\qquad 0 \leq r_i \leq 1 (i=1,2,...,N) \\ &\qquad 0 \leq s_i \leq 1 (i=1,2,...,N) \end{aligned} \tag{9}$$

where $\boldsymbol{r}$ and $\boldsymbol{s}$ denote the topological variable vectors and N denotes the number of elements; β is a function of the effective thermal stress tensor; C_{ijkl}^{H} is the effective elastic modulus of the metamaterial unit; $\underline{C}$ is the lower limit of the effective elastic modulus; W is the weight fraction, and $\overline{W}$ is its upper limit.

2.3 Energy level theory

In a phonon metamaterial, the scattering object is removed or changed to form a void, which affects the wave propagation. Owing to the destructive interference of scattered waves in the particular structure, the propagation is blocked and a bandgap is generated. In engineering, the study of phonon properties focuses on the width of the absolute bandgap. The elastic wave at any incident angle cannot propagate at a frequency in the absolute bandgap. The propagation of waves in solids can be expressed using Bloch's theorem. The governing equation of elastic wave motion is expressed as follows:

$$C_{ijkl}(\boldsymbol{q})\frac{\partial u_k(\boldsymbol{q},t)}{\partial t_l} = \rho(\boldsymbol{q})\frac{\partial^2 u_i(\boldsymbol{q},t)}{\partial t^2} \tag{10}$$

where $\boldsymbol{q} = (x, y, z)$ is the position vector, u_i is the displacement component, and ρ is the mass density. Based

on periodic boundary conditions, the displacement field of the angular frequency ω can be written as follows:

$$u(\boldsymbol{q},t) = u_i e^{i(\omega t - \boldsymbol{k}\cdot\boldsymbol{q})} \tag{11}$$

$$u(\boldsymbol{q}) = u_i(\boldsymbol{q} + R) \tag{12}$$

where $\boldsymbol{k}$ is the Bloch wave vector in the reduced Brillouin zone, and R is the translation periodicity of the metamaterial unit. For models without external forces, the discrete eigenvalue equation can be expressed as follows:

$$(K - \omega^2 M)u_i = 0 \tag{13}$$

where K and M are the stiffness and mass matrix, respectively. According to Eq. (10), the energy level diagram of the metamaterial can be obtained by sweeping the entire reduced Brillouin zone with the wave vector $\boldsymbol{k}$; thus, it can be assessed whether an absolute bandgap exists. The modal exchange caused by the structural parameters will lead to an absolute bandgap width between the fixed energy bands, which cannot reflect the phonon performance. Therefore, the ratio of the bandgap width (RBW) Q is defined as the value of the total absolute bandgap width divided by the maximum frequency in the previous 15th order energy band, which is used to evaluate the phonon properties of metamaterials.

3. Topology optimization of metamaterials

3.1. Conceptual design of metamaterial unit

In the NTE optimisation model, the elastic modulus constraint is $C_{ijkl}^{\mathrm{H}} \geqslant 0.1$ MPa ($ijkl$ = 1111,2222,3333). The weight fraction constraint is $W \leq 0.465$, which is half the weight of the design domain filled by the low thermal expansion material. To ensure the accuracy of the solution, the step size of each iteration was considered as $\Delta r_i = \Delta s_i = 0.01$. To improve the calculation efficiency, the conjugate gradient iteration method was adopted in the finite element analysis routines. Therefore, the lower limit of the topological variable could be set to zero without considering the numerical singularity. The elastic modulus, Poisson's ratio, density, and coefficient of thermal expansion are listed in Table 1.

Table 1. Material properties.

Material properties	Resin	Rubber
Elastic Modulus (MPa)	290	5
Poisson's ratio	0.3	0.47
Density (kg/m^3)	930	1117
CTE (/℃)	5×10^{-5}	1.5×10^{-4}

An optimization strategy is proposed to solve the design problem in the case wherein metamaterials are designed by two base materials whose elastic moduli are largely different. In the design of negative thermal expansion metamaterials, the large difference of the elastic modulus will make it difficult for the high CTE material to drive the structural deformation. Therefore, two virtual materials with similar elastic moduli were used to complete the initial optimization of the material distribution. The initial elastic modulus $E^{(1)}$ of the first material was set to 5 MPa. Then, in the optimization process, the elastic modulus was constantly updated in the order of [5, 25, 100, 290] MPa. Whenever the CTE was negative, $E^{(1)}$ was updated to the next elastic modulus until the material reached the actual elastic modulus. The topology optimization process with the iteration of the material properties is shown in Fig. 1. This strategy alleviates the phenomenon of the topological variables decaying too fast in the early stage of optimization and, to some extent, reduces the discontinuous structure in the results.

The design domain of metamaterials was limited for the convenience of observation and manufacturing. The design domain is shown in Fig. 2(a). To prevent the local optimal solution, a three-dimensional initial

configuration was obtained based on the combination of topological features and the rotation of the two-dimensional initial configuration, as shown in Appendix A1. The feasibility of the two-dimensional configuration was verified [62]. The initial configuration was symmetric in three directions and consisted of a material with low thermal expansion. The optimisation was realised through the ICM-mothed [37, 39] and numerical homogenisation method [63, 64] in MATLAB.

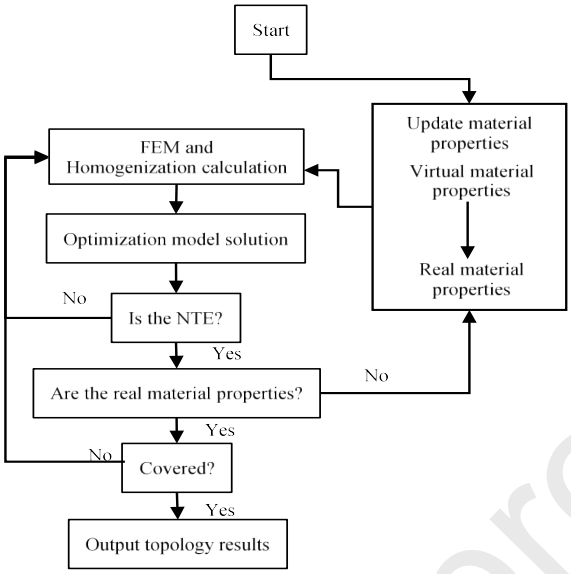

Fig. 1. Flow chart of topology optimization for material attribute iteration.

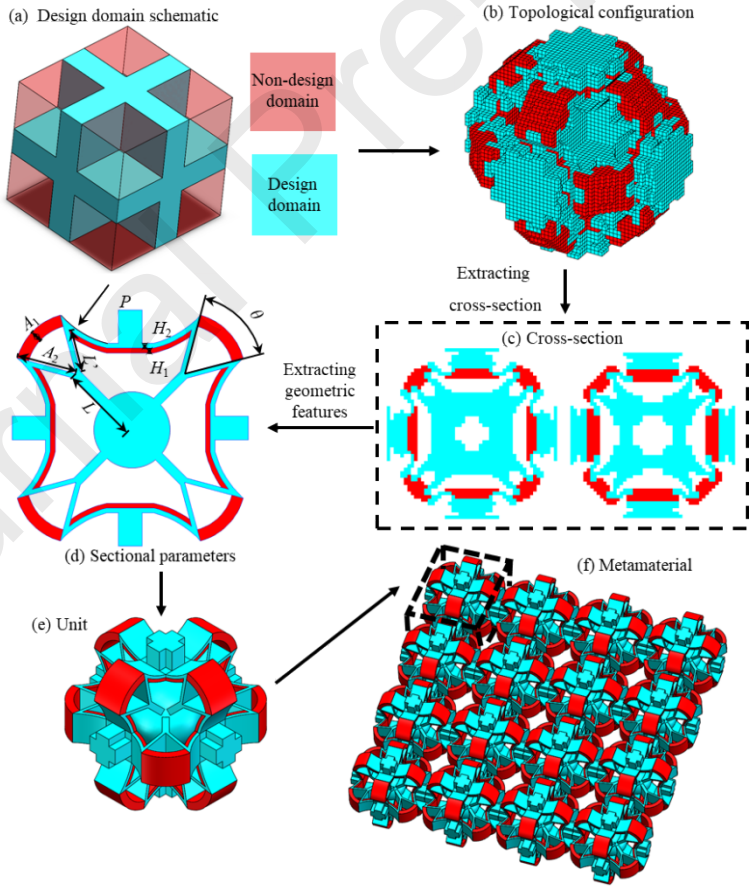

Fig. 2. (a) The transparent red areas are the non-design domain, and the sky-blue area is the design domain; (b) topology optimization configuration; (c) cross-section of topology optimization configuration; (d) parameterized cross-sections; (e) metamaterial unit; (f) metamaterials.

The optimisation results and process of feature extraction are shown in Fig. 2. The topological configuration in Fig. 2(b) was captured to obtain the two-dimensional feature cross-section shown in Fig. 2(c). The red

part indicates the material with high CTE, and the blue part indicates the material with low CTE. The common features of the topological cross-sections were extracted to establish the parameterized structure, as shown in Fig. 2(d). There are five parameters, namely, A, H, P, L, and θ, with the greatest impact on geometry. Here, A is the ratio of the red beam thickness A_1 to the outer radius A_2; H is the ratio of the high CTE beam thickness H_1 to the low CTE beam thickness H_2 at the double-layer beam; P denotes the curvature of the double beam; L is the rod length, and the sum of L and L' is set to 5 mm to avoid an aberrant structure; θ is the opening angle. The engineering drawings of all parameters in the structure are presented in Appendix A2. The metamaterial unit shown in Fig. 2(e) was obtained by rotating the two-dimensional cross-section. Finally, the metamaterials shown in Fig. 2(f) were obtained by arraying the units. As can be seen, the unit mainly consists of a bimaterial frame outside of the metamaterial and a central solid sphere. The thermal expansion deformation effect was mainly driven by the material in the outer red area. The internal sphere exerts significant influence on the dynamic performance and minor influence on the thermal expansion performance of the metamaterial.

3.2 Numerical simulation analysis

The negative thermal expansion properties of the metamaterial were verified by conducting a finite element simulation. The size of each unit was 10 mm×10 mm×10 mm. The array metamaterial contained 16 units. The thermal expansion behaviour was observed under the temperature of 100 °C. The negative expansion deformation of the metamaterials and three-dimensional unit deformation that occurred when the temperature increased are shown in Fig. 3(a) and (b). The displacement nephogram is shown in Fig. 3(c).

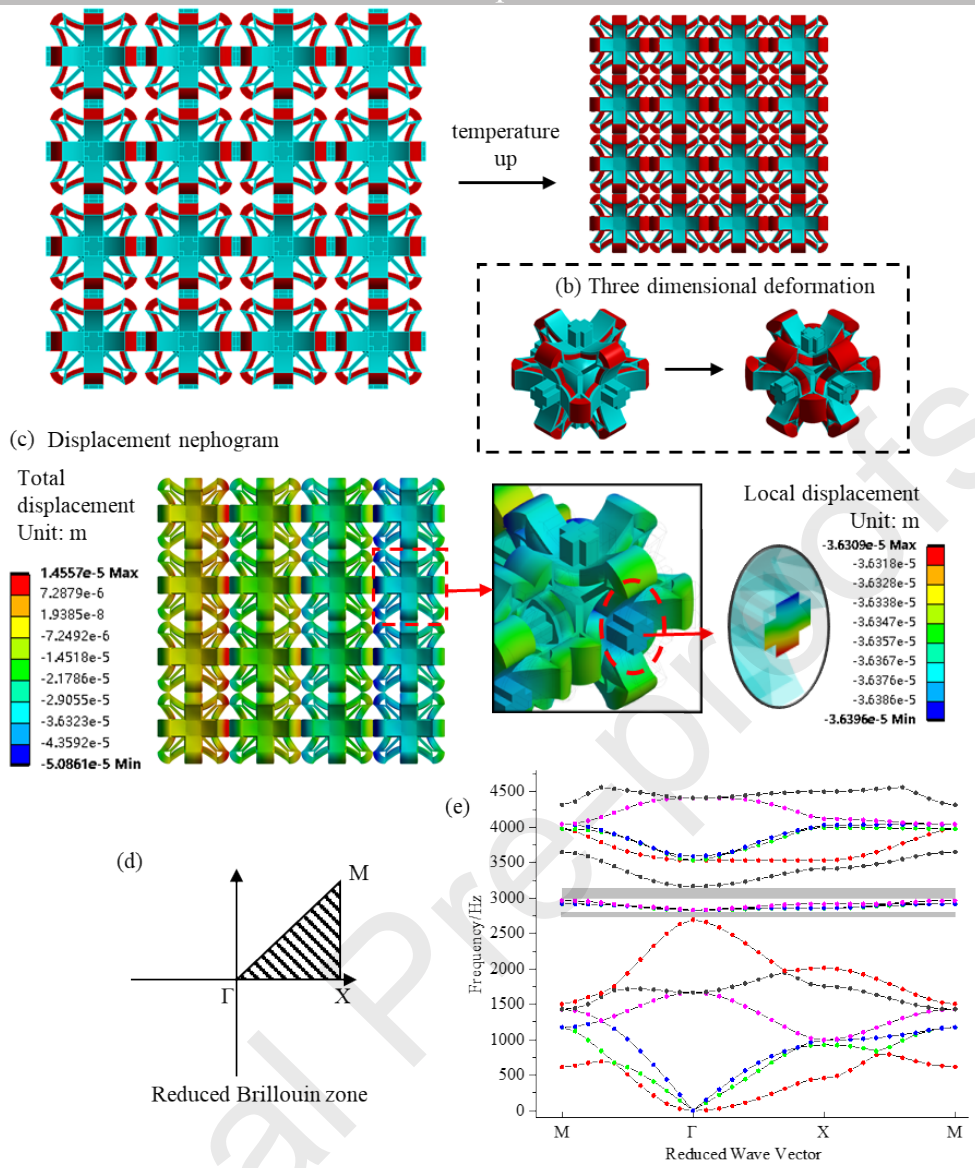

Fig. 3. Numerical simulation: (a) schematic diagram of metamaterial deformation under heat; (b) displacement nephogram; (c) simplified triangular Brillouin region; (d) dispersion curve and bandgap.

As can be seen, the structure contracted inward when the temperature increased, and the effective CTE of the metamaterial was -9.0875×10^{-6}/ °C. The results reveal that the proposed method is effective in the design of NTE metamaterials. Because the design of anisotropic NTE metamaterials is easier compared with that of isotropic NTE metamaterials, this method can be effectively used to design both isotropic and anisotropic metamaterials.

In accordance with the symmetry of the structure, the wave vector $\boldsymbol{k}$ swept the reduced Brillouin region, as shown in Fig. 3(d). Because the structure is designed to regulate low-frequency mechanical waves, the first 15 order energy bands were selected for analysis. The characteristic frequency of the structure was calculated using COMSOL, and the dispersion curve is shown in Fig. 3(e). The energy level diagram shows that the structure has two narrow absolute bandgaps. To achieve better thermal expansion performance and a larger bandgap width, a parameter optimisation method was used to carry out detailed optimisation.

4. Surrogate model-based optimization

4.1. Parametric analysis

The influences of the above-mentioned parameters on the CTE and RBW were investigated by changing every single parameter while keeping the other parameters unchanged. To prevent the interference of the structure, the ranges of the geometrical parameters were set to $A \in [0.2, 0.8]$, $H \in [0.5, 2.5]$, $P \in [0, 0.3]$, $L \in [1, 4]$mm, and $\theta \in [25, 55]°$. A reference structure was designed with A=0.5, H=1.2, P=0.15, L=2.5 mm, and θ=40°. To illustrate the influence of the geometrical parameters on the structural performance, seven sample points were taken for each parameter. The variables were compared by normalising the parameters, with 0 to 1 as the abscissa. The sample point data are presented in Appendix A3.

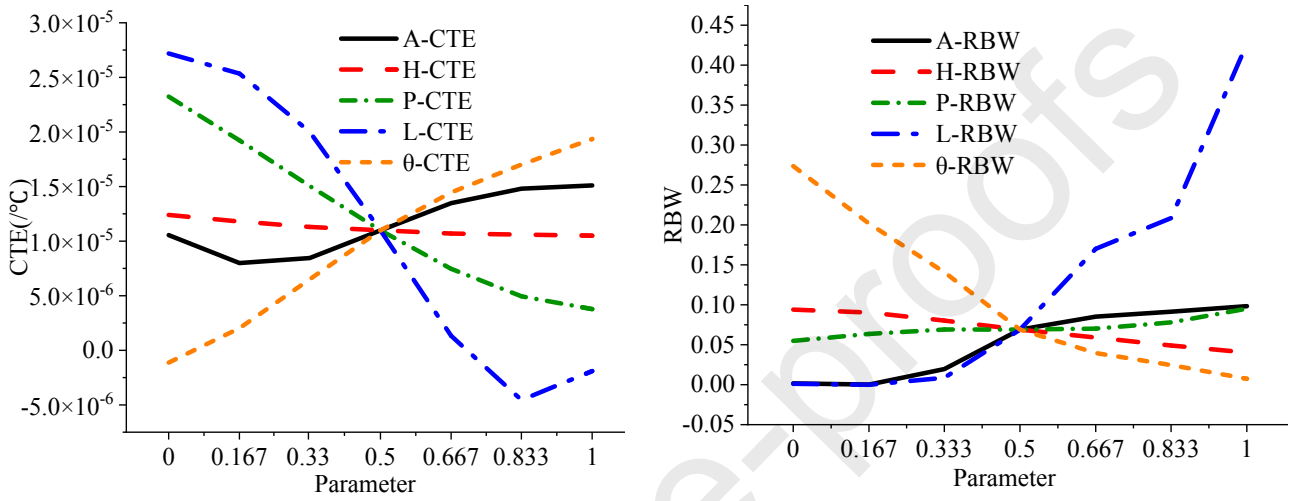

Fig. 4. (a) Variation curves of CTE for different parameters; (b) variation curves of RBW for different parameters.

Figure.4(a) shows that the CTE is positively correlated with A and θ, while the CTE is negatively correlated with parameters L, P, and H. The CTE obeys the rule of the cubic function with the change of parameter L. Additionally, the NTE structure with the minimum CTE of -4.54×10^{-6}/℃ can be obtained when L=0.35 mm. The effect of A on the structure resembles a sinusoidal function. The relationship between CTE and other parameters is approximately linear. In the above-mentioned structure, the NTE performance can be realized only by adjusting parameters L and θ. Figure 4(b) shows the value of RBW with different A, H, P, L, and θ. The RBW is positively correlated with parameters A, P, and L, while the RBW is negatively correlated with parameters H and θ. Parameter L plays a decisive role in bandgap formation. When L was close to 1 mm, a bandgap did not exist. When L=4 mm, the RBW reached 42.7% and the bandgap width was 2342 Hz. Regardless of how P and H change, there are always bandgaps and the bandgap width slightly changes.

The geometric parameters L and θ influenced the contributions of other parameters to the mechanical properties. The arc length of the double-layer beam increased when the length L increased, and this improved the influence of parameters P and H. However, when the length L decreased, the influence of P and H on the mechanical properties was reduced. Additionally, parameter θ affected other parameters. When θ decreased, the arc length of the double-layer beam increased, which improved the influence of P and H on the structure. However, when this angle increased, the influence of P and H on the structure was reduced. These analyses suggest that L and P are the two dominant parameters of both CTE and RBW, while the influence of parameter H is minor. Therefore, it is necessary to increase the range of parameter H while avoiding excessive structural deformities.

4.2. Response surface methodology

The response surface methodology (RSM) [65–67] was used to optimise the geometrical parameters and the influence of the geometrical parameters on the structural properties was investigated. The magnitude of the regression coefficient P_j was used to quantify the importance of each parameter. The magnitude order influence of the parameters on the regression coefficient was avoided by normalising the partial regression coefficient. The two endpoint values of each parameter were selected for fitting calculation, and the sample point data are presented in Appendix A4. The normalised regression coefficients are shown in Fig. 5.

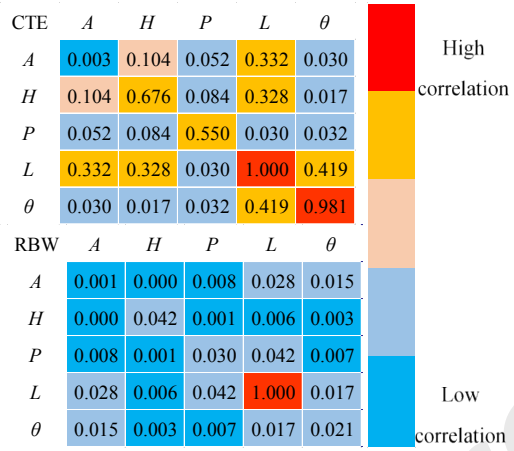

Fig. 5. Normalized regression coefficient. On the main diagonal, red indicates that the parameter exerts stronger influence on the metamaterial properties, while the blue square indicates that the parameter has weaker influence. On the non-diagonal, the red square indicates that the corresponding two parameters have higher correlation, while the blue square indicates lower correlation.

Table 2. Linear regression coefficient and ranking.

Parameters	P_j (CTE)	Ranking (CTE)	P_j (RBW)	Ranking (RBW)
A	8.58%	5	3.85%	4
H	19.94%	3	3.85%	5
P	12.32%	4	6.52%	2
L	34.77%	1	81.10%	1
θ	24.38%	2	4.68%	3

Table 2 presents the linear regression coefficient and ranking of A, H, P, L, and θ to the structure's CTE and RBW. The influence of the parameters on CTE is L, θ, H, P, and A in descending order. The influence of the parameters on RBW is L, P, θ, A, and H in descending order.

Considering the importance ranking and correlation, two parameters L and θ were first selected as the optimisation parameters. The 25 groups of the sample points were used to fit the quartic function. The sample points and the response surface fitting formulas are presented in Appendix A5. It was found that the optimised parameters L are all taken on the boundary, which means that an increase in L can simultaneously minimise the thermal expansion coefficient and maximise the bandgap. This means that the parameter L takes 4 mm as the optimal solution, and is not a suitable variable for optimisation. Therefore, two optimisation models were established to obtain a more extreme CTE with variables P and θ, and obtain more wideband gaps with variables H and P. The sample points and response surface fitting formulas are presented in Appendices A6 and A7, respectively.

4.3. Optimization results and discussion

Different constraint-solving models were adopted to investigate the various obtained results. In the optimisation model with variables P and θ, the obtained parameters were P=0.237 and θ=50.00. A unit with a CTE of -1.29×10^{-5}/ °C and RBW of 0.179 was obtained. In the optimisation model with variables H and

P, the obtained parameters were H=0.5 and P=0.0765. A unit with a CTE of -3.41×10^{-5}/ °C and RBW of 0.4[illegible] was obtained.

Figure 6(a) shows that the optimised metamaterial with variables *P* and *θ* has a wide bandgap between the 10th and 11th energy bands. The CTE reached the highest value of -1.29×10^{-5}/ °C. The total bandgap width of the metamaterial reached 928 Hz from 3027 Hz to 3955 Hz. The frequency response functions (FRF) of the metamaterials were obtained by arraying six units and applying excitation, as shown in Fig. 6(b). The vibration waves with frequencies close to the absolute bandgap were blocked. Additionally, because the excitation wave was unidirectional, the vibrations of the frequencies in the vicinity of 1500 Hz to 2200 Hz were also blocked. This phenomenon is also reflected in the energy level diagram. Figure 6(c) shows that the optimised metamaterial with variables *H* and *P* has many bandgaps. The CTE is -3.41×10^{-6}/°C. The widest bandgap width of the metamaterial reached 1855 Hz from 2469 Hz to 4324 Hz. The FRF of the metamaterials was obtained as shown in Fig. 6(d). The blocked frequencies in Fig. 6(d) are the same as those in the energy-level diagram. The two above-mentioned FRFs verify the accuracy of the simulation of the energy level diagrams in this study.

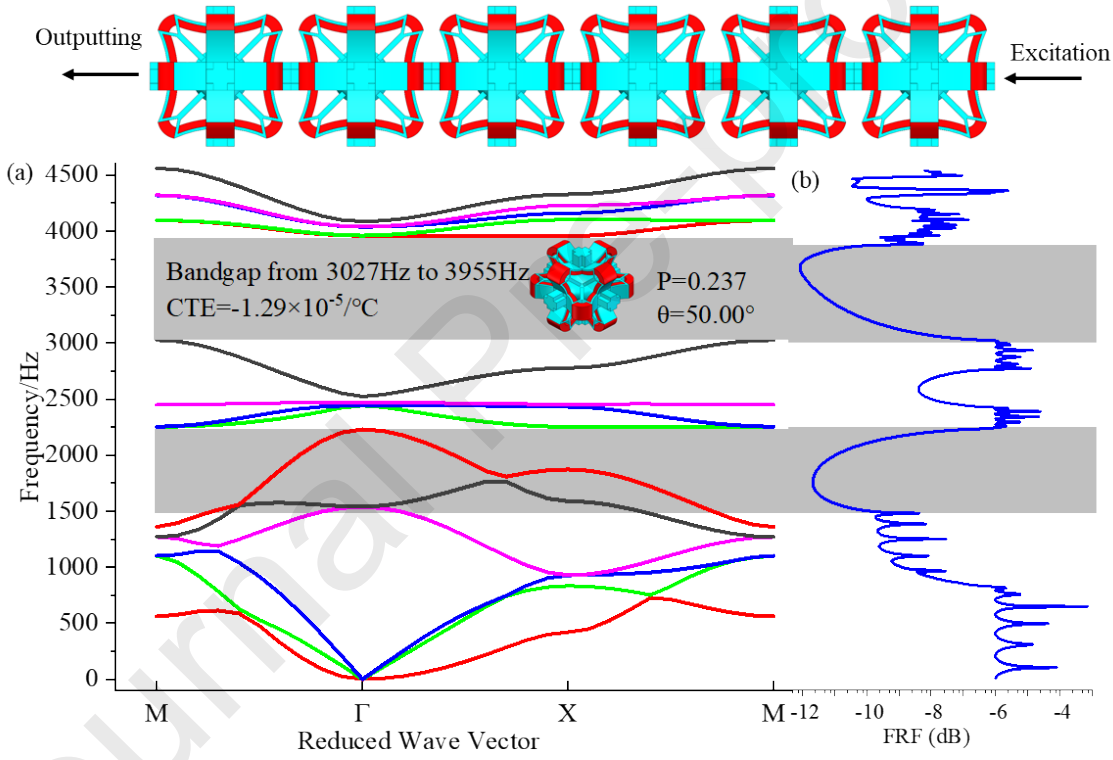

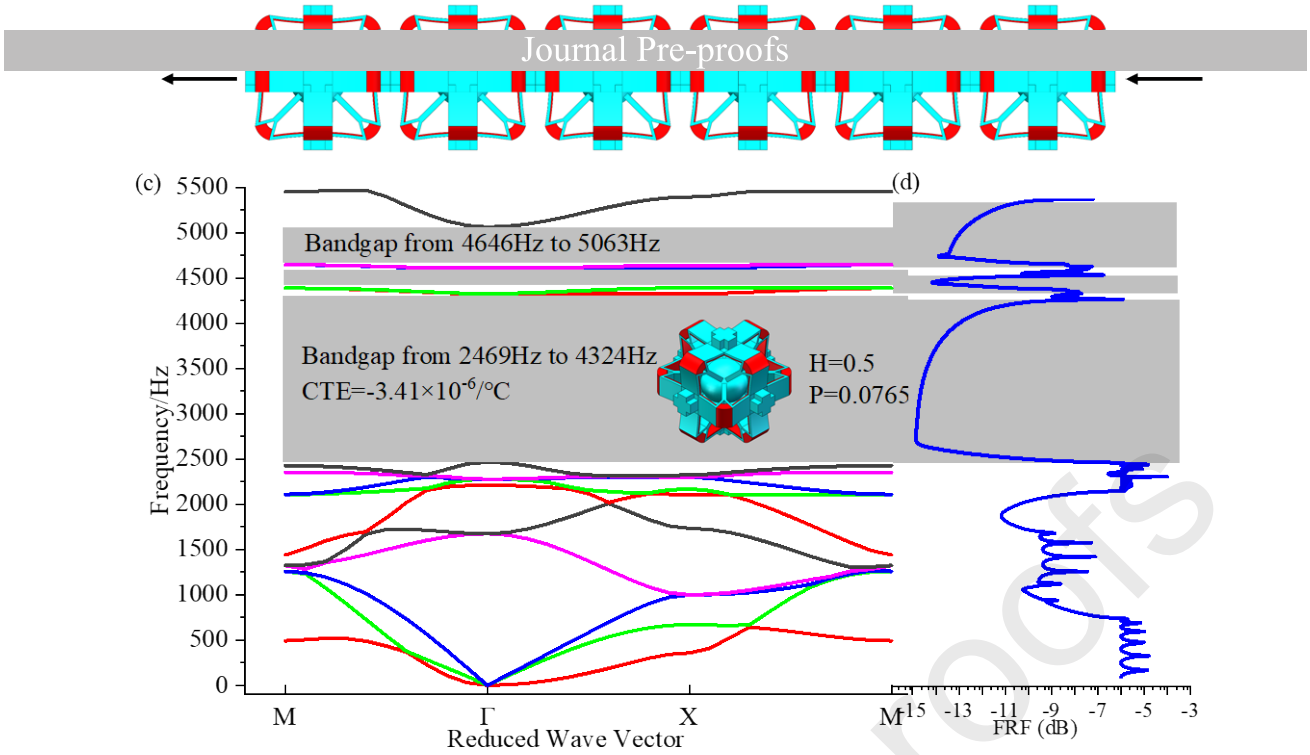

Fig. 6. Optimized bandgap diagram and frequency response functions: (a) band diagram of structures with extremely negative CTE; (b) frequency response function corresponding to the metamaterial in (a); (c) band diagram of structures with wide bandgap; (d) frequency response function corresponding to metamaterial in (c).

Based on the above-mentioned results, both the CTE and RBW ranges can be obtained for the considered structure. By changing the parameters, the CTE can be adjusted from -1×10^{-5}/°C to 2.5×10^{-5}/°C, and the RBW can also be changed from 0 to 0.5. When negative thermal expansion is required, the metamaterial without a bandgap shown in Fig. 7(c) can be optimised to have a wide bandgap, as shown in Fig. 7(a). When the thermal expansion property was not considered, the structure could achieve an extremely wide bandgap, as shown in Fig. 7(b). From the statistics of the above-mentioned simulation results, the CTE and RBW ranges of the considered structure can be obtained as shown in Fig. 7(d).

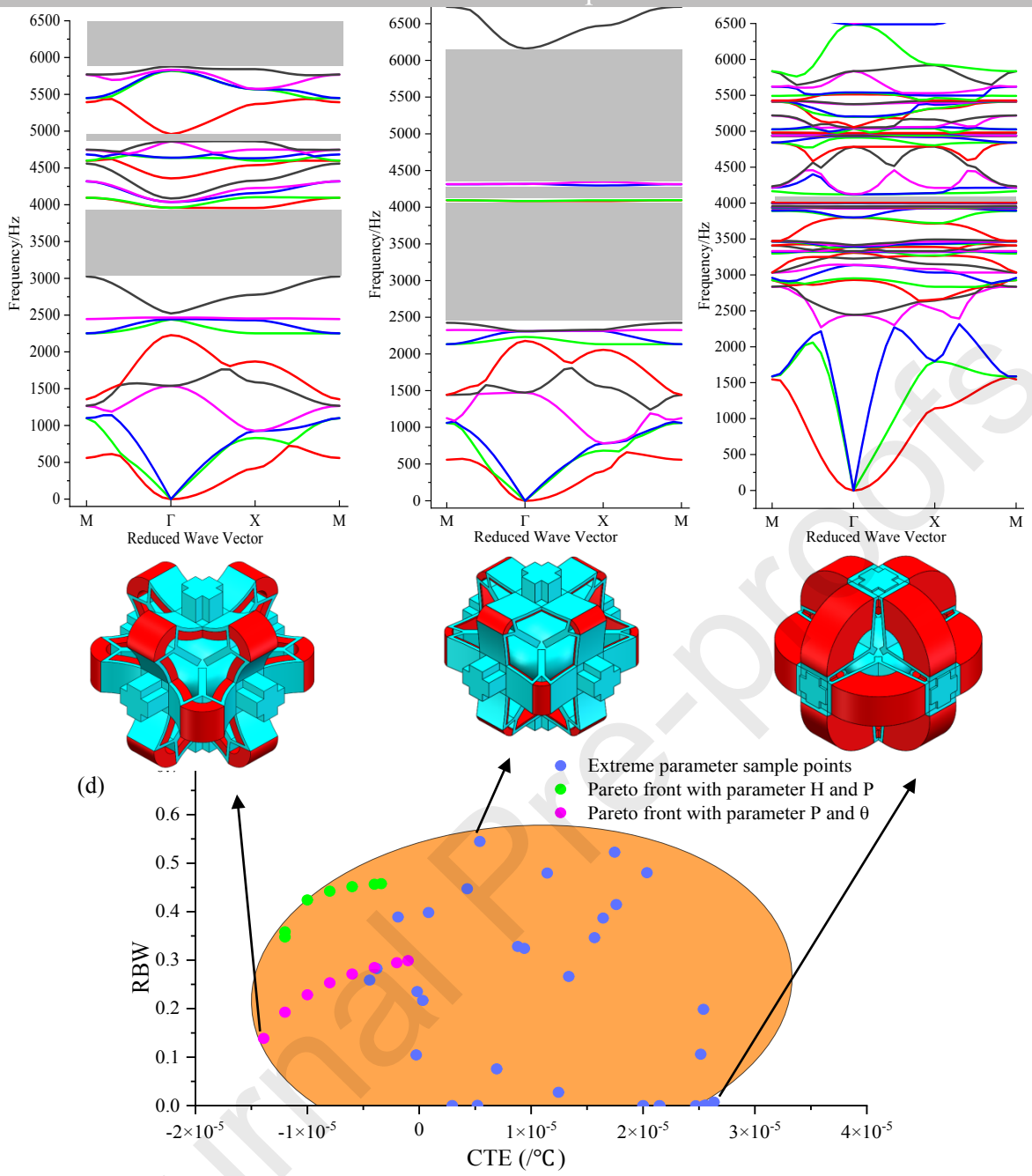

Fig. 7. Energy level diagram of different structural parameters: (a) energy level diagram of structure with negative thermal expansion property and bandgap; (b) energy level diagram of wide bandgap structure without negative thermal expansion property; (c) energy level diagram of structure without negative thermal expansion property and few bandgaps; (d) range of CTE and RBW. The blue points indicate the sample points discussed in Section 4.2; the red points indicate the two optimized points; the orange part is the range of RBW and CTE corresponding to this structure type.

5. Conclusion

This study developed a new design optimisation methodology for creating three-dimensional microstructured metamaterials and achieved both negative thermal expansion and phononic bandgaps by integrating the ICM topology optimisation method with a surrogate model-based optimisation approach. First, a three-dimensional metamaterial microstructure was designed to exhibit negative thermal expansion using the ICM-based topology optimisation method. Secondly, the conceptual structure from the topology optimisation was reconstructed, and a response surface methodology was applied to further optimise the

parameters of the topological design and achieve phononic bandgaps subject to negative thermal expansion. The negative thermal expansion and phonon bandgap properties of the designed metamaterials were demonstrated using the finite element method, and the influence of the geometric parameters on the properties was discussed. Two metamaterials with different thermal expansion coefficients and phonon bandgaps were designed. The boundary between the coefficient of thermal expansion and the phonon bandgap of the metamaterial was predicted through the statistical analysis of numerical examples. Thus, it was proven that optimised metamaterials have great potential for use in the control of thermal deformation and phonons. Topology optimisation has been shown to have unique advantages in the investigation of novel geometries for various structures and materials, and surrogate model-based optimisation can further improve the local properties of topologically optimised design. By combining the two different optimisation methods into a new design system, new materials with enhanced manufacturability and performance can be obtained. This study provides a general design methodology for the systematic development of a broad range of multifunctional metamaterials.

Acknowledgements

This research was supported by the National Natural Science Foundation of China (11872080) and Natural Science Foundation of Beijing, China (3192005), as well as the Australian Research Council (ARC) - Discovery Projects (DP210101353).

Declaration of interests

The authors declare that they have no known competing financial interests or personal relationships that could have influenced the work reported in this paper.

References

[1]

[2] H. Gharibi, A. Bahrami. Phononic crystals for sensing FAMEs with demultiplexed frequencies, J Mol Liq. 305 (2020):112841.

[3] C. Ma, J. Liu, S. Wang. Thermal error compensation of linear axis with fixed-fixed installation, Int J Mech Sci. 175 (2020):105531.

[4] D. Zhengchun, Z. Mengrui, W. Zhiguo, et al. Design and application of composite platform with extreme low thermal deformation for satellite, Compos Struct. 152 (2016):693-703.

[5] L. Li, X. Gang, Z. Sun, et al. Design of phononic crystals plate and application in vehicle sound insulation, Adv Eng Softw. 125 (2018):19-26.

[6] C. Qin, Z. Xu, M. Xia, et al. Design and optimization of the micro-vibration isolation system for large space telescope, J Sound Vib. 482 (2020):115461.

[7] D. Wu, L. Lin, H. Ren. Thermal/vibration joint experimental investigation on lightweight ceramic insulating material for hypersonic vehicles in extremely high-temperature environment up to 1500 °C, Ceram Int. 46 (2020):14439-47.

[8] H. Zhang, X.G. Guo, J. Wu, et al. Soft mechanical metamaterials with unusual swelling behavior and tunable stress-strain curves, Sci Adv. 4 (2018):r8535.

[9] J. Qu, M. Kadic, A. Naber, et al. Micro-Structured Two-Component 3D Metamaterials with Negative Thermal-Expansion Coefficient from Positive Constituents, Sci Rep-UK. 7 (2017):40643.

[10] L. Wu, B. Li, J. Zhou. Isotropic Negative Thermal Expansion Metamaterials, ACS Appl Mater Inter. 8 (2016):17721-17727.

[11] C.S. Ha, E. Hestekin, J. Li, et al. Controllable thermal expansion of large magnitude in chiral negative Poisson's ratio lattices: Controllable thermal expansion in chiral negative Poisson's ratio lattices, Phys Status Solidi B. 252 (2015):1431-1434.

[12] R. Lakes. Cellular solids with tunable positive or negative thermal expansion of unbounded magnitude, Appl Phys Lett. 90 (2007):221905.

[13] R. Lakes. Cellular solid structures with unbounded thermal expansion, J Mater Sci Lett. 15 (1996):475-477.

[14] H. Yu, W. Wu, J. Zhang, et al. Drastic tailorable thermal expansion chiral planar and cylindrical shell structures explored with finite element simulation, Compos Struct. 210 (2019):327-338.

[15] W. Wu, W. Hu, G. Qian, et al. Mechanical design and multifunctional applications of chiral mechanical metamaterials: A review, Mater Design. 180 (2019):107950.

[16] K. Wei, X. Xiao, J. Chen, et al. Additively manufactured bi-material metamaterial to program a wide range of thermal expansion, Mater Design. 198 (2021):109343.

[17] M. Chen, M. Fu, L. Lan, et al. A novel 3D structure with tunable Poisson's ratio and tailorable coefficient of thermal expansion based on a tri-material triangle unit, Compos Struct. 253 (2020):112803.

[18] K. Wei, Y. Peng, K.Y. Wang, et al. Three dimensional lightweight lattice structures with large positive, zero and negative thermal expansion, Compos Struct. 188 (2018):287-96.

[19] L. Ai, X.L. Gao. Metamaterials with negative Poisson's ratio and non-positive thermal expansion, Compos Struct. 162 (2017):70-84.

[20] N.M.A. Palumbo, C.W. Smith, W. Miller, et al. Near-zero thermal expansivity 2-D lattice structures: Performance in terms of mass and mechanical properties, Acta Mater. 59 (2011):2392-2403.

[21] C.A. Steeves, S.L. Dos Santos E Lucato, M. He, et al. Concepts for structurally robust materials that combine low thermal expansion with high stiffness, J Mech Phys Solids. 55 (2007):1803-1822.

[22] L.V. Gibiansky, S. Torquato. Thermal expansion of isotropic multiphase composites and polycrystals, J Mech Phys Solids. 45 (1997):1223-1252.

[23] R.K. Oruganti, A.K. Ghosh, J. Mazumder. Thermal expansion behavior in fabricated cellular structures, Mat Sci Eng A-Struct. 371 (2004):24-34.

[24] H. Li, H. Li, M. Xiao, et al. Robust topology optimization of thermoelastic metamaterials considering hybrid uncertainties of material property, Compos Struct. 248 (2020):112477.

[25] S. Watts, D.A. Tortorelli. Optimality of thermal expansion bounds in three dimensions, Extreme Mech Lett. 12 (2017):97-100.

[26] A. Takezawa, M. Kobashi. Design methodology for porous composites with tunable thermal expansion produced by multi-material topology optimization and additive manufacturing, Compos Part B-Eng. 131 (2017):21-29.

[27] M.P. Bendsøe, N. Kikuchi. Generating optimal topologies in structural design using a homogenization method, Comput Method Appl M. 71 (1988):197-224.

[28] M. Zhou, G.I.N. Rozvany. The COC algorithm, Part II: Topological, geometrical and generalized shape optimization, Comput Method Appl M. 89 (1991):309-336.

[29] M.P. Bendsoe, O. Sigmund. Material interpolation schemes in topology optimization, Arch Appl Mech. 69 (1999):635-54.

[30] O. Sigmund. A 99 line topology optimization code written in Matlab, Struct Multidisc Optim. 21 (2001):120-127.

[31] Z. Luo, N. Zhang, Y. Wang, et al. Topology optimization of structures using meshless density variable approximants, Int J Numer Meth Eng. 93 (2013):443-464.

[32] M.Y. Wang, X.M. Wang, D.M. Guo. A level set method for structural topology optimization, Comput Methods Appl Mech Engrg. 192 (2003):227-246.

[33] G. Allaire, F. Jouve, A. Toader. Structural optimization using sensitivity analysis and a level-set method, J Comput Phys. 194 (2004):363-393.

[34] [illegible] 76 (2008):1-26.

[35] A. Takezawa, S. Nishiwaki, M. Kitamura. Shape and topology optimization based on the phase field method and sensitivity analysis, J Comput Phys. 229 (2010):2697-2718.

[36] X. Guo, W. Zhang, W. Zhong. Doing Topology Optimization Explicitly and Geometrically-A New Moving Morphable Components Based Framework, J Appl Mech-T ASME. 81 (2014).

[37] H.L. Ye, Z.J. Dai, W.W. Wang, et al. ICM method for topology optimization of multimaterial continuum structure with displacement constraint, Acta Mech Sinica-PRC. 35 (2019):552-562.

[38] Y.K. Sui, H.L. Ye, X.R. Peng. Topological optimization of continuum structure with global stress constraints based on ICM method: Springer Netherlands; 2006.

[39] H.L. Ye, N. Chen. Topological optimization of plate subjected to linear buckling constraints based on Independent Continuous Mapping method, Appl Mech Mater. 602-605 (2014):139-143.

[40] X.R. Peng, Y.K. Sui. Lightweight topology optimization with consideration of the fail-safe design principle for continuum structures, Eng Optimiz. 53 (2021):32-48.

[41] N. Xu, H. Liu. A novel 3-D structure with tunable Poisson's ratio and adjustable thermal expansion, Compos Commun. 22 (2020):100431.

[42] X. Li, L.B. Gao, W.Z. Zhou, et al. Novel 2D metamaterials with negative Poisson's ratio and negative thermal expansion, Extreme Mech Lett. 30 (2019):100498.

[43] Y. Wang, J. Gao, Z. Luo. Level-set topology optimization for multimaterial and multifunctional mechanical metamaterials, Eng Optimiz. 49 (2017):22-42.

[44] R. Tao, L. Xi, W. Wu, et al. 4D printed multi-stable metamaterials with mechanically tunable performance, Compos Struct. 252 (2020):112663.

[45] Z. Ren, L. Ji, R. Tao, et al. SMP-based multi-stable mechanical metamaterials: From bandgap tuning to wave logic gates, Extreme Mech Lett. 42 (2021):101077.

[46] R. Tao, L. Ji, Y. Li, et al. 4D printed origami metamaterials with tunable compression twist behavior and stress-strain curves, Compos Part B-Eng. 201 (2020):108344.

[47] X. Lv, S. Xu, Z. Huang, et al. A shape memory alloy-based tunable phononic crystal beam attached with concentrated masses, Phys Lett A. 384 (2020):126056.

[48] Y. Chen, B. Wu, J. Li, et al. Low-frequency tunable topological interface states in soft phononic crystal cylinders, Int J Mech Sci. 191 (2021):106098.

[49] L. He, Z. Wen, Y. Jin, et al. Inverse design of topological metaplates for flexural waves with machine learning, Mater Design. 199 (2021):109390.

[50] L. Yao, D. Zhang, K. Xu, et al. Topological phononic crystal plates with locally resonant elastic wave systems, Applied Acoustics. 177 (2021):107931.

[51] Muhammad, C.W. Lim, J.T.H. Li, et al. Lightweight architected lattice phononic crystals with broadband and multiband vibration mitigation characteristics, Extreme Mech Lett. 41 (2020):100994.

[52] D. Qi, H. Yu, W. Hu, et al. Bandgap and wave attenuation mechanisms of innovative reentrant and anti-chiral hybrid auxetic metastructure, Extreme Mech Lett. 28 (2019):58-68.

[53] H. Dong, S. Zhao, Y. Wang, et al. Topology optimization of anisotropic broadband double-negative elastic metamaterials, J Mech Phys Solids. 105 (2017):54-80.

[54] S. Huo, J. Chen, H. Huang, et al. Experimental demonstration of valley-protected backscattering suppression and interlayer topological transport for elastic wave in three-dimensional phononic crystals, Mech Syst Signal Pr. 154 (2021):107543.

[55] T. Delpero, S. Schoenwald, A. Zemp, et al. Structural engineering of three-dimensional phononic crystals, J Sound Vib. 363 (2016):156-165.

[56] H. Dong, S. Zhao, Y. Wang, et al. Robust 2D/3D multi-polar acoustic metamaterials with broadband double negativity, J Mech Phys Solids. 137 (2020):103889.

[57] L. Chen, Y. Guo, H. Yi. Optimization study of bandgaps properties for two-dimensional chiral phononic crystals base on lightweight design, Phys Lett A. 388 (2021):127054.

[58] K. Wang, Y. Liu, B. Wang. Ultrawide band gap design of phononic crystals based on topological optimization, Physica B. 571 (2019):263-272.

[59] X.K. Han, Z. Zhang. Bandgap design of three-phase phononic crystal by topological optimization, Wave Motion. 93 (2020):102496.

[60] H. Dong, S. Zhao, X. Miao, et al. Customized broadband pentamode metamaterials by topology optimization, J Mech Phys Solids. 152 (2021):104407.

[61] X. Li, S. Ning, Z. Liu, et al. Designing phononic crystal with anticipated band gap through a deep learning based data-driven method, Comput Method Appl M. 361 (2020):112737.

[62] H.L. Ye, X. Zhang, N. Wei. Topology Optimization Design of Adjustable Thermal Expansion Metamaterial Based on Independent Continuous Variables, Int J Appl Mech. 13 (2021):2150032. https://doi.org/10.1142/S1758825121500320.

[63] K. Liu, A. Tovar. An efficient 3D topology optimization code written in Matlab. Struct Multidisc Optim. 50 (2014):1175-1196.

[64] [illegible] 5.

[65] G.G. Wang, S. Shan. Review of metamodeling techniques in support of engineering design optimization, J Mech Design. 129 (2007):370-380.

[66] Y. Zhang, H.L. Ye, B.W. Li, et al. Mechanical behavior of composite bistable shell structure and surrogate-based optimal design, Struct Multidisc Optim. (2021).

[67] H.L. Ye, Y. Zhang, Q.S. Yang, et al. Optimal design of a three tape-spring hinge deployable space structure using an experimentally validated physics-based model, Struct Multidisc Optim. 56 (2017):973-989.